Integrating Leveling and InSAR Networks for the Monitoring of Subsidence Due to Gas Extraction

Dennis Odijk

Summary

Although leveling is a very precise technique for geodetic deformation monitoring, it is quite expensive and time-consuming. InSAR is a relatively new technique for precise deformation monitoring and has some important advantages compared to leveling: the high spatial resolution of the data and the relatively low costs of the technique. In this article both techniques are considered for the estimation of subsidence due to gas extraction. Simulations demonstrate that although InSAR has the capability to provide sub-cm accuracy for this type of deformation monitoring, an integration with leveling is the best choice as long as InSAR is not at a fully reliable level.

Zusammenfassung

Das klassische Nivellement zur geodätischen Überwachung von Deformationen ist mit hohen Kosten und großem Zeitaufwand verbunden. Bei InSAR handelt es sich dagegen um eine relativ neue Technik, die im Vergleich mit dem Nivellement als Vorteil insbesondere eine sehr hohe räumliche Auflösung bei relativ geringen Kosten bietet. In diesem Aufsatz werden beide Techniken für die Analyse von Bodensenkungen in Folge von Gasextraktion im Bereich des Groninger Gasfeldes betrachtet. Anhand von Simulationsrechnungen lässt sich zeigen, dass eine Integration von InSAR und Nivellement der beste Weg ist, obwohl InSAR im Prinzip bereits Deformationsanalysen mit sub-cm Genauigkeit ermöglicht.

1 Introduction

Due to its situation below sealevel, the monitoring of land subsidence is an important issue in the Netherlands. In the northeast, the exploitation of the large Groningen gas field and its smaller adjacent fields has resulted in smooth subsidence bowls up to several kilometers in diameter with a velocity of typically one centimeter per year. Since the beginning of gas production in the 1960s spirit leveling surveys have been carried out on a regular basis. Although this technique allows for the detection of very small surface deformations, it is rather time-consuming and thus expensive. The introduction of space-geodetic techniques like GPS and the interferometric use of Synthetic Aperture Radar (InSAR) has offered new opportunities for precise deformation monitoring. In particular, using the InSAR technique at relatively low costs (when compared to leveling) relatively large subsidence areas can be monitored. InSAR provides vertical displacements between coherent points in two SAR acquisitions (images). Additional benefits of InSAR are that it

is not necessary to physically access the deformation area and the high spatial and temporal density of the data. Besides, sub-centimeter accuracy has been reported for InSAR-derived surface deformations, see e.g. Massonnet and Feigl (1998).

In this article it is investigated to what extent an integration of leveling observations and vertical displacement data derived from InSAR results in a more efficient deformation monitoring system than based on leveling data only. GPS-derived vertical displacements are not considered here because of their lower spatial density compared to InSAR. Simulations have been carried out to study the performance of an integration of leveling and InSAR vertical displacement data for subsidence estimation. Aspects that play a role in these design computations are the spatial and temporal density of the leveling and InSAR networks, in combination with the assumptions concerning the stochastic properties of the observations. Before discussing these simulations, in the next sections an extensive overview is provided of the procedure we applied for the mathematical modeling of land subsidence due to gas extraction.

2 A spatio-temporal model for land subsidence

The developed procedure for the monitoring in gas field areas is based on a *spatio-temporal* modeling of the subsidence. This section describes this modeling in detail.

2.1 Vertical deformations in gas field areas

In this paper we consider *slow-term* land subsidence due to gas extraction, which ranges from a few millimeters up to a few centimeters a year. However, a point in such a subsidence area may also be subject to movements due to other causes (not due to gas extraction). In presence of all kinds of deformations, the height of a point i at time t, denoted as $H_{i,t}$ can be written as the following function (Kenselaar and Quadvlieg 2001):

$$\underline{H}_{i,t} = H_{i,t_0} + \underline{g}_{i,t-t_0} + \underline{\eta}_{i,t},\tag{1}$$

where t_0 denotes the start time of the deformation, H_{i,t_0} the height of the point before or at the beginning of deformation (»initial« height), $g_{i,t-t_0}$ the motion of the point due to gas extraction, and $\eta_{i,t}$ the motions of the point that are *not* caused by gas extraction. Motions not caused by gas extraction are usually due to local effects (for example ground water variations).

The underscore in Eq. (1) emphasizes the stochastic nature of a variable. The deformation due to gas extraction, i. e. $\underline{g}_{i,t-t_0}$, is assumed as a stochastic process, since in practice it is usually impossible to completely model it by a deterministic function. In Sect. 2.2 this so-called *trend-signal* modeling is discussed in detail. The deformation of the points that is not caused by gas extraction, $\underline{\eta}_{i,t}$ in Eq. (1), is also assumed as a stochastic process. Suppose that we have two epochs, denoted as t_l and t_m, then the following covariance function is used to describe the temporal behavior of local point instabilities:

$$\sigma_{\eta_{i,t_l}\eta_{i,t_m}} = \sigma_{b_i}^2(\min[t_l,t_m] - t_1), \tag{2}$$

where $\min[\cdot,\cdot]$ denotes the minimum operator, t_1 the first epoch at which the measurements are obtained and σ_{b_i} a point-specific standard deviation (also referred to as *point noise*). From Eq. (2) note that the point instabilities are allowed to become larger with time. In fact, they are modeled as a *random-walk* process. These point instabilities are uncorrelated in space assumed.

2.2 Modeling deformations due to gas extraction

In our procedure for subsidence estimation the vertical deformation due to gas extraction is decomposed into a deterministic *trend*, denoted as z, plus a stochastic *signal*, denoted as $\underline{\xi}$:

$$\underline{g}_{i,t-t_0} = z_{i,t-t_0} + \underline{\xi}_{i,t-t_0}. \tag{3}$$

The purpose of the estimation procedure is to solve for this sum of trend and signal. For the application of slow-term subsidence in gas field areas spatiotemporal models have proven to be valid for both trend and signal.

2.2.1 Modeling the deformation trend

It is known that subsidence of the surface above deep gas reservoirs shows strong coherence, both in space and time. In among others (Houtenbos 2000) it was shown that for the deformation trend therefore smooth 7-parameter spatiotemporal subsidence bowls can be applied. In this paper we adopt this method. The subsidence trend is modeled as a superposition of n_B bowls, in which the center of each bowl subsides with an unknown but constant velocity. In addition, it is assumed that this subsidence velocity *exponentially* decreases with increasing distance from the center of the bowl. Mathematically, we may then write the trend $z_{i,t-t_0}$ in Eq. (3) as:

$$z_{i,t-t_0} = \sum_{B=1}^{n_B} z_{i,t-t_{0,B}}, \text{ where } z_{i,t-t_{0,B}}$$
$$= \begin{cases} 0 & \text{for } t \leq t_{0,B} \\ v_B(t-t_{0,B})\exp\{-\tfrac{1}{2}r_{i,B}^2\} & \text{for } t \geq t_{0,B} \end{cases}, \tag{4}$$

where $t_{0,B}$ denotes the start time of subsidence of bowl B, v_B the subsidence velocity in the center of this bowl,

and $r_{i,B}$ the standardized radius from the center of this bowl to point i. The subsidence velocity at point i can be computed as $v_B \exp\{-\tfrac{1}{2}r_{i,B}^2\}$. It is assumed that each bowl has an *ellipsoidal* shape in the horizontal plane, such that the standardized radius can be written as follows:

$$\begin{aligned} r_{i,B}^2 &= \left(\frac{(x_i-x_{c,B})\sin\phi_B+(y_i-y_{c,B})\cos\phi_B}{a_B}\right)^2 \\ &+ \left(\frac{(x_i-x_{c,B})\cos\phi_B-(y_i-y_{c,B})\sin\phi_B}{b_B}\right)^2, \end{aligned} \tag{5}$$

where (x_i, y_i) denote the (known) horizontal coordinates of point i, $(x_{c,B}, y_{c,B})$ the coordinates of the center of bowl B, (a_B, b_B) the half long respectively half short axes of this bowl, and ϕ_B the argument of the long axis of this bowl. To recover the deformation trend we need to determine seven parameters for each bowl: the two *temporal* parameters v_B and $t_{0,B}$, plus the five *spatial* parameters $(x_{c,B}, y_{c,B})$, a_B, b_B and ϕ_B.

2.2.2 Modeling the deformation signal

Unfortunately, for many gas fields it is not possible to describe the land subsidence due to gas extraction using only the trend model. For example, for the large and complex Groningen gas field in the Netherlands a deterministic trend only turns out to be insufficient (Houtenbos 2000). Hence, the signal term $\xi_{i,t-t_0}$ in Eq. (3) accounts for the imperfection of the adopted trend model with respect to the actual land subsidence. This term is also referred to as *model noise*, see e. g. Kenselaar and Quadvlieg (2001). In our procedure these discrepancies are modeled as a stochastic process with both temporal and spatial components. Conform Houtenbos (2000) it is assumed that in the temporal domain the signal can be described by a *random-walk* process, while in the spatial domain it can be modeled by a *Gaussian* covariance function, this latter function is an exponential depending on the squared distance between points, see e. g. Wackernagel (1998). Suppose we have two points, denoted as i and j, and two epochs, denoted as t_l and t_m, then the *covariance* between the signal at point i at epoch t_l and the signal at point j at epoch t_m is modeled as:

$$\sigma_{\xi_{i,t_l}\xi_{j,t_m}} = \sigma_g^2(\min[t_l,t_m] - t_1)\exp\{-(l_{ij}/L_g)^2\}. \tag{6}$$

In this covariance function σ_g denotes the standard deviation of the signal, t_1 the first measurement epoch, l_{ij} the horizontal distance between points i and j and L_g the correlation distance of the signal.

3 Observation equations

To estimate subsidence by means of the trend-signal model, in this section it will be connected to two types of observations: spirit leveling measurements and vertical displacements as derived from modern space-geodetic

techniques like InSAR or GPS. This section deals with their observation equations.

3.1 Leveling data

In case of conventional leveling, an observed height difference between two points i and j on epoch t, denoted as $\underline{w}_{ij,t}$, can be written as:

$$\underline{w}_{ij,t} = -\underline{H}_{i,t} + \underline{H}_{j,t} + \underline{\varepsilon}_{ij,t}^{w}, \tag{7}$$

where $\underline{H}_{i,t}$ denotes the height of point i at time t and $\underline{H}_{j,t}$ the height of point j at time t. Random measurement errors are contained in the term $\underline{\varepsilon}_{ij,t}^{w}$. By inserting Eq. (1) into Eq. (7), we may rewrite the observation equation as function of initial heights, vertical deformations and a term due to noise:

$$\begin{aligned} lll\underline{w}_{ij,t} =\ & -H_{i,t_0} + H_{j,t_0} - \underline{g}_{i,t-t_0} + \underline{g}_{j,t-t_0} \\ & -\underline{\eta}_{i,t} + \underline{\eta}_{j,t} + \underline{\varepsilon}_{ij,t}^{w}. \end{aligned} \tag{8}$$

Decomposing the vertical deformation due to gas extraction into a trend and signal term, see Eq. (3), we obtain:

$$\begin{aligned} lll\underline{w}_{ij,t} =\ & -H_{i,t_0} + H_{j,t_0} - z_{i,t-t_0} + z_{j,t-t_0} \\ & \underbrace{-\underline{\xi}_{i,t-t_0} + \underline{\xi}_{j,t-t_0} - \underline{\eta}_{i,t} + \underline{\eta}_{j,t} + \underline{\varepsilon}_{ij,t}^{w}}_{\underline{e}_{ij,t}^{w}}, \end{aligned} \tag{9}$$

where all stochastic terms, i. e. the deformation signal (ξ), point noise (η) and measurement noise (ε) are collected in one random error term, denoted as $\underline{e}_{ij,t}^{w}$. Note that since the mathematical expectation of all three individual components is zero, also the combined noise term has zero expectation. A common assumption for the *measurement noise* of leveling data is to assume them normally (Gaussian) distributed and uncorrelated, both in space and time. The measurement noise of a leveling observation is proportional to the length of the measured trajectory, denoted as s_{ij}:

$$\sigma_{\varepsilon_{ij,t}^{w}}^{2} = \sigma_{w_t}^{2} s_{ij}. \tag{10}$$

In case of precise leveling data, the standard deviation is usually within the interval $0.5 < \sigma_{w_t} < 1 \text{ mm}/\sqrt{\text{km}}$.

3.2 Vertical displacement data

3.2.1 The general case

Vertical displacements derived from space-geodetic techniques like InSAR or GPS are nothing else than temporal differences of two sets of heights of a collection of points. In case of InSAR we may have vertical deformations for the time interval between two SAR acquisitions. In case of GPS we may have the differences between the heights of the stations of a permanent network at two epochs.
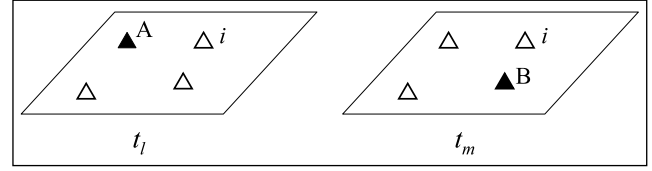
Fig. 1: Set of heights at two epochs. At epoch t_l the heights are relative to the height of point A: $h_{i,t_l}^{A} = h_{i,t_l} - h_{A,t_l}$, while at epoch t_m they are relative to point B: $h_{i,t_m}^{B} = h_{i,t_m} - h_{B,t_m}$.

Note that a set of heights within a SAR image or corresponding to GPS points at a certain epoch are never absolute heights, but always *relative* to a (non-stochastic assumed) reference point. Since it is not always known which point is selected as reference and whether this point is also reference for another epoch, in our estimation procedure the heights of the reference points are additional unknown parameters. Suppose that at epoch t_l we have a set of heights which are relative to point A, denoted as $\underline{h}_{i,t_l}^{A}$, while at epoch t_m we have a set of heights which are relative to point B, denoted as $\underline{h}_{i,t_m}^{B}$ (see Fig. 1), then for a point i the difference between the two heights, denoted as $v_{i,t_l t_m}$, can be written as:

$$\underline{v}_{i,t_l t_m} = -\underline{h}_{i,t_l}^{A} + \underline{h}_{i,t_m}^{B} + \underline{\varepsilon}_{i,t_l t_m}^{v}, \tag{11}$$

where the measurement noise of this vertical displacement observation is contained in the term $\underline{\varepsilon}_{i,t_l t_m}^{v}$. Inserting $\underline{h}_{i,t_l}^{A} = \underline{h}_{i,t_l} - h_{A,t_l}$ and $\underline{h}_{i,t_m}^{B} = \underline{h}_{i,t_m} - h_{B,t_m}$ yields:

$$\underline{v}_{i,t_l t_m} = -\underline{h}_{i,t_l} + \underline{h}_{i,t_m} + h_{A,t_l} - h_{B,t_m} + \underline{\varepsilon}_{i,t_l t_m}^{v}, \tag{12}$$

where h_{A,t_l} denotes the height of *reference* A at time t_l and h_{B,t_m} the height of *reference* B at time t_m. However, this observation equation cannot be used yet to estimate deformations, since one should realize that GPS or InSAR-derived heights are *geometric* heights, i. e. they are heights above a certain reference ellipsoid, e. g. WGS84. When InSAR- or GPS-derived vertical displacement data are integrated with leveling data, the observation equation should – like the leveling observation equation (7) – be expressed as *orthometric* heights, i. e. heights with respect to the *geoid*. Both geometric heights and orthometric heights are however connected as follows, for example for the heights of point i at epoch t:

$$h_{i,t} = H_{i,t} + N_{i,t}. \tag{13}$$

Here $N_{i,t}$ denotes the height of the geoid above the reference ellipsoid (*geoid undulation*), see Fig. 2. The observation equation as function of the orthometric heights of point i now becomes:

$$\begin{aligned} lll\underline{v}_{i,t_l t_m} =\ & -\underline{H}_{i,t_l} + \underline{H}_{i,t_m} - N_{i,t_l} + N_{i,t_m} \\ & + h_{A,t_l} - h_{B,t_m} + \underline{\varepsilon}_{i,t_l t_m}^{v}, \end{aligned} \tag{14}$$

This observation equation can be simplified, since it is normally allowed to assume the geoid undulation as a
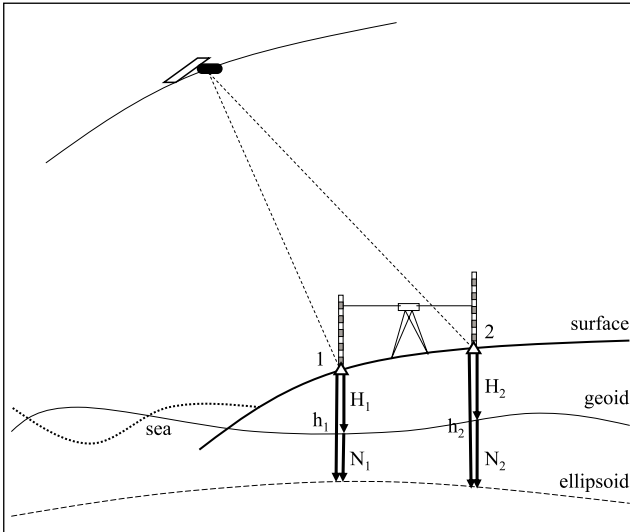
Fig. 2: The relation between the orthometric height H_i and the geometric height h_i is given by the geoid undulation N_i.

constant in time, i. e. $N_{i,t_l} = N_{i,t_m}$. The observation equation then reduces to:

$$\underline{v}_{i,t_l t_m} = -\underline{H}_{i,t_l} + \underline{H}_{i,t_m} + h_{A,t_l} - h_{B,t_m} + \underline{\varepsilon}^v_{i,t_l t_m}. \qquad (15)$$

This observation equation can in a next step be expressed as function of the vertical deformations by inserting expressions for $\underline{H}_{i,t_l}$ and $\underline{H}_{i,t_m}$, conform Eq. (1):

$$lll\underline{v}_{i,t_l t_m} = -\underline{g}_{i,t_l-t_0} + \underline{g}_{i,t_m-t_0} + h_{A,t_l} - h_{B,t_m}$$
$$-\underline{\eta}_{i,t_l} + \underline{\eta}_{i,t_m} + \underline{\varepsilon}^v_{i,t_l t_m}. \qquad (16)$$

Note that the initial height of point i is eliminated in this equation. Decomposing the vertical deformation due to gas extraction into a trend and signal term, conform Eq. (3), we obtain the following observation equation:

$$\underline{v}_{i,t_l t_m} = -z_{i,t_l-t_0} + z_{i,t_m-t_0} + h_{A,t_l} - h_{B,t_m}$$
$$\underbrace{-\underline{\xi}_{i,t_l-t_0} + \underline{\xi}_{i,t_m-t_0} - \underline{\eta}_{i,t_l} + \underline{\eta}_{i,t_m} + \underline{\varepsilon}^v_{i,t_l t_m}}_{\underline{e}^v_{i,t_l t_m}}. \qquad (17)$$

Similar to the leveling observation equation, the random error term $\underline{e}^v_{i,t_l t_m}$ in Eq. (17) is a combination of deformation signal, point noise and measurement noise. As mentioned, there are no initial heights in this observation equation, in contrast to the leveling observation equation (9). On the other hand, in observation equation (17) we have to account for a difference in reference heights A and B. It should be noted that also the *same* reference height can be used at both epochs. Suppose that this is point A, then we have to account for the height difference of point A in time: $h_{A,t_l} - h_{A,t_m}$. It can also be true that we a priori know that this reference point is *stable*. In that case the difference in reference heights completely disappears from observation equation (17).

3.2.2 InSAR-derived vertical displacement data

In this paper we focus on the integration of leveling data with InSAR-derived vertical displacement data, rather than GPS-derived vertical displacements. This choice is not only motivated by the cost aspect, but also by the spatial density of InSAR-derived deformation data (up to 1600 points/km²), which is much higher than of GPS data. The temporal density of InSAR-derived data is lower than of (permanent) GPS data, because of the revisit interval of the SAR sensors onboard radar satellites, which can be more than one month. However, this is not really an issue for slow-term deformation problems as due to gas extraction. The collection of InSAR-derived deformations for one time interval is referred to as a *vertical displacement map*. In order to make assumptions on the *measurement noise* of InSAR-derived vertical displacements, it is necessary to briefly explain the way these data are generated from raw InSAR observations.

Generation of an InSAR displacement map

Synthetic Aperture Radar sensors measure both magnitude and phase of the transmitted electromagnetic signal that is backscattered from the earth's surface. The phase measurement is used to derive information on heights and deformations of the terrain. This phase represents a combination of the distance between the SAR antenna and the surface, and the surface scattering effect. If a second SAR data set is collected, then from comparing the phase of the second image with the phase of the first, an *interferogram* can be formed. The basic principle of interferometric SAR is that if the surface characteristics are identical for both images, the phase difference between corresponding pixels in both images only accounts for the distance-dependent component. The surface scattering effects will be the same when the distance between the orbital positions of the radar (called the *baseline*) is small. This is established by making benefit of the repeating constellation of SAR sensors onboard radar satellites. For deformation applications the baseline should ideally be zero in order to eliminate topographic information from the interferogram (since this may bias true surface deformations). However, due to satellites drifting from their nominal orbits, baselines will be non-zero. Fortunately, the interferogram can be corrected for topographic information using an external digital elevation model (DEM). As a result, a *differential* interferogram is obtained that only contains the topographic *changes* that occurred between the two SAR acquisitions.

Limitations of InSAR

Using the described procedure a vertical displacement map with a very high resolution (about $25 \times 25\,\text{m}^2$) can be obtained. Since the accuracy of the phase measurement is a fraction of (half) the radar wavelength (2–3 mm for distance measurements of typical radars), this in principle allows for mm-accuracy of vertical deformations

(Hanssen 2001). There are however some important limitations (Hanssen and Ferretti 2002):

- The phase measurements are ambiguous: only the fractional phase can be measured while the number of whole cycles is unknown.

- Inaccuracies in the *satellite orbits* cause baseline errors which result in increased phase noise.

- Differences in *atmospheric conditions* between the two SAR acquisitions cause spatially correlated errors in the phase measurements.

- The surface backscattering characteristics within one resolution cell (pixel) change in time, which causes weak phase correlation (interferometric coherence) between both images. This loss of coherence is known as *temporal decorrelation* and makes InSAR unsuitable for, for example, vegetated areas.

For the design studies described in Sect. 6 it is however assumed that the first two limitations are overcome. It is namely assumed that for every point in the displacement map the phase can be successfully *unwrapped* and that absolute phases are obtained. In addition, it is assumed that errors due to the satellite orbits are absent by using *precise orbits*.

Conventional vs. permanent-scatterer InSAR

The two other limitations of the InSAR technique, i. e. the atmospheric errors and the temporal decorrelation, are currently important topics of research. Recently the so-called *permanent-scatterers* InSAR technique has been developed to isolate coherent pixels and to solve the atmospheric errors (Ferretti et al. 2001). These coherent pixels (the permanent scatterers) are usually stable natural reflectors, like roofs of buildings or rocks. Although the locations of the permanent scatterers cannot be predicted, their density will vary between 50 and 400 points/km^2. Despite this lower density compared to the conventional InSAR technique in which just two acquisitions are used to compute a displacement map (about 1600 points/km^2), it is still much higher than obtained with traditional geodetic techniques like leveling and GPS. Drawback is that for this technique many, e. g. more than 30, SAR images are needed, from which the atmospheric errors are estimated (Hanssen and Ferretti 2002). For the simulations described in Sect. 6 it is assumed that we have InSAR-derived displacement maps based on the conventional approach which can be biased by atmospheric errors, as well as maps based on the permanent-scatterer approach free of atmospheric errors.

Assumptions InSAR measurement noise

In this article the atmospheric errors – when present – are modeled as random errors, which means that they are part of the InSAR measurement noise term $\underline{\varepsilon}^v_{i,t_l t_m}$ in Eq. (17). As a consequence, the measurement noise becomes

spatially correlated. It is assumed that the covariance between points i and j in each map can be described by

$$\sigma_{v_i v_j} = \sigma_\phi^2 \delta_{ij} + \sigma_a^2 \exp\{-(l_{ij}/L_a)^2\}. \tag{18}$$

In this covariance function σ_ϕ^2 denotes the variance of the phase measurement and the Delta function is defined as $\delta_{ij} = 1$ for $i = j$ and $\delta_{ij} = 0$ for $i \neq j$. The atmospheric variance is denoted as σ_a^2 and the correlation distance of the atmospheric errors as L_a. The variance of each point in a displacement map due to measurement noise follows thus as $\sigma_\phi^2 + \sigma_a^2$. In absence of atmospheric errors, we set $\sigma_a^2 = 0$. Whereas the phase standard deviation is at mm-level, the atmospheric standard deviation is typical of the order of 1 cm. The correlation distance of the atmospheric errors can be a few km.

When different maps have a common start date or end date, the InSAR measurement noise should also address *temporal* correlation. This correlation is positive when two maps have either the same start or end date (in case of so-called *single-master* interferograms; see Hanssen et al. 2003), whereas the correlation is negative when the end date of the first map corresponds to the start date of the second map (in case of so-called *cascaded* interferograms; see ibid). Taking these considerations into account, the covariance between point i of a displacement map over time interval (t_l, t_m) and point j of a displacement map over time interval (t_f, t_g) can be written as:

$$\sigma_{\varepsilon^v_{i,t_l t_m} \varepsilon^v_{j,t_f t_g}} = \begin{cases} \sigma_{v_i v_j}, & \text{if } t_l = t_f \wedge t_m = t_g \\ \frac{1}{2}\sigma_{v_i v_j}, & \text{if } t_l = t_f \wedge t_m \neq t_g, \\ & \quad \text{or } t_l \neq t_f \wedge t_m = t_g \\ -\frac{1}{2}\sigma_{v_i v_j}, & \text{if } t_l \neq t_g \wedge t_m = t_f, \\ & \quad \text{or } t_l = t_g \wedge t_m \neq t_f \\ 0, & \text{otherwise.} \end{cases} \tag{19}$$

4 Mathematical model

4.1 Functional model

For deformation estimation, the observation equations derived in Sect. 3 are connected to the seven trend parameters per subsidence bowl through Eqs. (4) and (5). These trend parameters are computed by means of an *integrated least-squares adjustment* of all leveling and/or vertical displacement data simultaneously. Since both Eqs. (4) and (5) are nonlinear, we first need to *linearize* the observation equations. For the linearization we need approximate values of all unknown parameters. After linearization, we may reformulate the linearized observations equations as a Gauss-Markov model:

$$E\left\{\underbrace{\begin{bmatrix} \Delta\underline{w} \\ \Delta\underline{v} \end{bmatrix}}_{\underline{y}}\right\} = \underbrace{\begin{bmatrix} WA_{hgt} & WA_{sub} & 0 \\ 0 & VA_{sub} & A_{sht} \end{bmatrix}}_{A} \underbrace{\begin{bmatrix} \Delta H_{t_0} \\ \Delta p \\ \Delta h_{AB} \end{bmatrix}}_{x}, \tag{20}$$

where:

$E\{\cdot\}$: mathematical expectation operator

Δw : »observed-minus-computed« vector of leveling data

Δv : »observed-minus-computed« vector of vertical displacement data

ΔH_{t_0} : incremental vector of leveling »null« heights

Δp : incremental vector of subsidence parameters

Δh_{AB} : incremental vector of reference height differences (»shifts«)

W : matrix to transform heights to leveling height differences

V : matrix to transform heights to vertical displacement height differences

A_{hgt} : matrix selecting null heights for leveling observations

A_{sub} : matrix with coefficients due to linearization of bowl equations

A_{sht} : matrix needed for the parameterization of shift parameters.

Model (20), referred to as the *functional* model, distinguishes between three groups in parameter vector x. The first group, ΔH_{t_0}, contains the *initial or »null« heights* corresponding to the leveling points. It is not possible to estimate all null heights in the adjustment: we have to constrain one of these heights to its a priori value (or zero). The choice of this so-called *S-basis* (see Baarda 1973) is arbitrary since it does not influence the estimated subsidence. It is also not necessary that this height remains stable. The second group of parameters are the *subsidence parameters*. For n_B bowls we have $\Delta p = (\Delta p_1^T, \ldots, \Delta p_{n_B}^T)^T$, where $\Delta p_B = (\Delta v_B, \Delta t_{0,B}, \Delta x_{c,B}, \Delta y_{c,B}, \Delta a_B, \Delta b_B, \Delta \phi_B)^T$ is the vector of seven parameters of the Bth bowl. The subsidence parameters are of course the parameters we are primarily interested in. In this context it should be noted that for the start time of subsidence, $\Delta t_{0,B}$, being estimable, we need data of *before* the gas production started. Otherwise it should be constrained to an a priori value. The third parameter group, Δh_{AB}, contains the differences in reference heights (*shifts*) of the vertical displacement data between different epochs. Not the individual reference heights are estimable in the adjustment, but only combined terms, for example $h_{A,t_l} - h_{B,t_m}$ (see Eq. (17)). So for each set (or *map*) of vertical displacement observations *one* shift is parameterized.

Note from the design matrix A of model (20) that the partial design matrices corresponding to the leveling null heights (A_{hgt}) and the subsidence parameters (A_{sub}) are pre-multiplied by matrices W and V. Both matrices, which only contain ones and zeros, are introduced to perform *differencing* operations. The reason for introducing these matrices is that it is easier to set up the partial design matrices at the absolute point and epoch level, than relative in space (in case of leveling), or relative in time (in case of vertical displacement observations). Both matrices W and V only contain (minus) ones and zeros. This pre-multiplication is not necessary for the partial design

matrix of the shift parameters, since the estimable shift parameters can be regarded as parameters that are already differenced. Hence, matrix A_{sht} is a simple vector having ones at all entries.

To set up the partial design matrix of the subsidence parameters, A_{sub}, we also need the *horizontal coordinates* of all involved leveling and vertical displacement points. In order to perform an integral adjustment of both types of observations, these horizontal positions must be defined in one and the same coordinate system. If this is not the case, coordinate transformations should be applied.

4.2 Stochastic model

The stochastic properties of the leveling and vertical displacement data are modeled in the *stochastic model*, i.e. the variance-covariance (vc-) matrix. This reads:

$$D\left\{\underbrace{\begin{bmatrix} \Delta \underline{w} \\ \Delta \underline{v} \end{bmatrix}}_{\underline{y}}\right\} = \underbrace{\begin{bmatrix} Q_\varepsilon^w & 0 \\ 0 & Q_\varepsilon^v \end{bmatrix} + \begin{bmatrix} W \\ V \end{bmatrix} (Q_\eta + Q_\xi) \begin{bmatrix} W \\ V \end{bmatrix}^T}_{Q_y},$$

(21)

where:

$D\{\cdot\}$: mathematical dispersion operator
Q_ε^w : vc-matrix of the leveling data
Q_ε^v : vc-matrix of the vertical displacement data
Q_η : vc-matrix of the point instabilities
Q_ξ : vc-matrix of the deformation signal.

As shown, the vc-matrix of the observations consists of two parts: a block-diagonal part (left of the plus sign in Eq. (21)), and a part that consists of a multiplication of matrices (right of the plus sign). The first part models the measurement noise. Both measurement noise vc-matrices, Q_ε^w and Q_ε^v, are constructed using the covariance functions in Eqs. (10) and (19), respectively. The second part models both point noise and deformation signal. The point noise vc-matrix, Q_η, is created using the covariance function in Eq. (2), while the vc-matrix accounting for the deformation signal, Q_ξ, is filled using the covariance function in Eq. (6). Note that since the point noise is uncorrelated in space, there is no correlation between the leveling and vertical displacement data due to point noise (since it can be proved that $WQ_\eta V^T = 0$). Both types of observations become correlated however, because the spatially correlated deformation signal implies that $WQ_\xi V^T \neq 0$.

5 Estimation and testing procedure

A powerful consequence of formulating an integrated adjustment model (20) is that it enables *statistical hypothesis testing* of both leveling and vertical displacement data.

Note that the spatiotemporal subsidence model allows for testing on (gross) errors in the data even when there is no redundancy in the individual data sets. For example, when a simple leveling line is measured at two epochs, the individual »networks« do not have redundancy since no loops can be formed. Redundancy is however introduced when the two epochs are connected by means of the spatiotemporal model (provided that the start time of subsidence $\Delta t_{0,B}$ is constrained; otherwise at least three leveling epochs should be used). Statistical testing of the data of individual vertical displacement maps is impossible when no spatiotemporal model is used. In contrast to leveling the individual maps are not redundant and hence it is not possible to form loops or whatsoever. However, it is possible to test the data of an individual map when the spatiotemporal model is introduced (provided that the start time of subsidence $\Delta t_{0,B}$ is constrained; otherwise at least two maps should be used).

With the functional and stochastic models as specified in the previous section, the best fitting subsidence model is determined in a stepwise procedure of least-squares adjustment, statistical hypothesis testing and adaptation of both the data and the model. In each step the actual model and data (the so-called *null-hypothesis* model) are tested against a number of alternative hypotheses, each suggesting a specific model adaptation or possible error(s) in the data. For an overview of the alternative hypotheses relevant for subsidence monitoring we refer to Kenselaar (2001).

5.1 Solving the trend model

When the null-hypothesis is not rejected eventually, the least-squares solution for the unknown parameters of the trend model, denoted as $\hat{\underline{x}}$, plus its variance-covariance matrix, denoted as $Q_{\hat{x}}$, is obtained as:

$$\hat{\underline{x}} = \left(A^T Q_y^{-1} A \right)^{-1} A^T Q_y^{-1} \underline{y}, \quad Q_{\hat{x}} = \left(A^T Q_y^{-1} A \right)^{-1}. \tag{22}$$

The least-squares solution of the subsidence parameters is part of vector $\hat{\underline{x}}$. It reads $\hat{\underline{p}} = p^0 + \Delta \hat{\underline{p}}$, where p^0 is the vector of approximate values. Using the solution for the subsidence parameters, the least-squares solution for the trend at any arbitrary point and at any epoch (not necessarily at the locations of the measurement data or at the measurement epochs) is obtained by inserting the entries of $\hat{\underline{p}}$ into Eq. (4). For a point G at epoch t_n this solution is denoted as $\hat{\underline{z}}_{G,t_n-t_0}$.

5.2 Estimation of signal and total subsidence

In order to resolve the total subsidence at any point at any epoch, besides the trend also the signal needs to be solved, see Eq. (3). The signal is computed using the vector

of least-squares *residuals* of the trend model. This vector is computed as:

$$\hat{\underline{e}} = P_A^\perp \underline{y}, \tag{23}$$

where the orthogonal projector is computed as $P_A^\perp = I - A \left(A^T Q_y^{-1} A \right)^{-1} A^T Q_y^{-1}$. The least-squares solution of the signal at a point G at epoch t_n is now obtained as:

$$\hat{\underline{\xi}}_{G,t_n-t_0} = q_{\xi_{G,t_n-t_0}}^T M^T Q_y^{-1} \hat{\underline{e}}, \tag{24}$$

where $M^T = \left[W^T, \ V^T \right]$, and $q_{\xi_{G,t_n-t_0}}$ a vector accounting for the covariances between the signal at point G at epoch t_n and the signals at the observed points and epochs. In fact, this computation of the signal for a specific point at a specific epoch corresponds to least-squares *collocation*. With both trend and signal solved, the least-squares solution of the total subsidence easily follows as:

$$\hat{\underline{\vartheta}}_{G,t_n-t_0} = \hat{\underline{z}}_{G,t_n-t_0} + \hat{\underline{\xi}}_{G,t_n-t_0}. \tag{25}$$

When the subsidence is estimated in this way for a grid over the subsidence area, it is possible to create *contour maps* of the estimated/collocated subsidence.

6 Simulations

In order to gather experience into the estimability of a spatiotemporal subsidence bowl, some simulations were carried out. Goal of these design studies is to evaluate the performance of an integration of leveling and InSAR-derived vertical displacement data for subsidence estimation. Advantage of conducting simulations is that the performance of the different processing strategies can then easily be assessed by comparing the estimated subsidence with this ground truth. In practice the true subsidence is of course unknown and then it can be rather difficult to separate the subsidence due to gas extraction from the subsidence caused by other driving mechanisms (for example, ground water variations).

6.1 Simulated subsidence

The design studies described in this article are a continuation of the simulations described in Kenselaar and Martens (2000), in which only leveling measurements were used. In our design studies we simulated the same single subsidence bowl as in (ibid), but we also added a signal to the subsidence trend. This deformation signal was generated at a grid of 49×49 points over the subsidence area of 25×25 km, using the random generator of Matlab. For this stochastic process we assumed a standard deviation of $2 \, \text{mm}/\sqrt{\text{yr}}$ and a correlation distance of 3 km, see Eq. (6). These values can be expected in practice (Houtenbos 2000). Tab. 1 summarizes the characteristics of the simulated subsidence. Fig. 3 shows contour
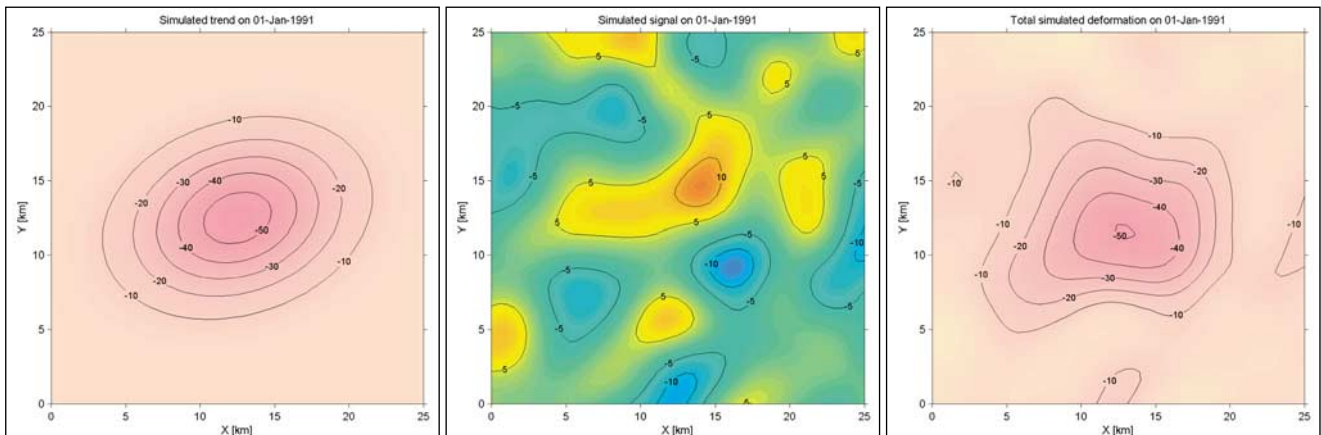
Fig. 3: Contour maps of simulated trend (left), signal (middle) and total deformation (sum of trend and signal; right) on 1 January 1991. All contour labels are in mm.
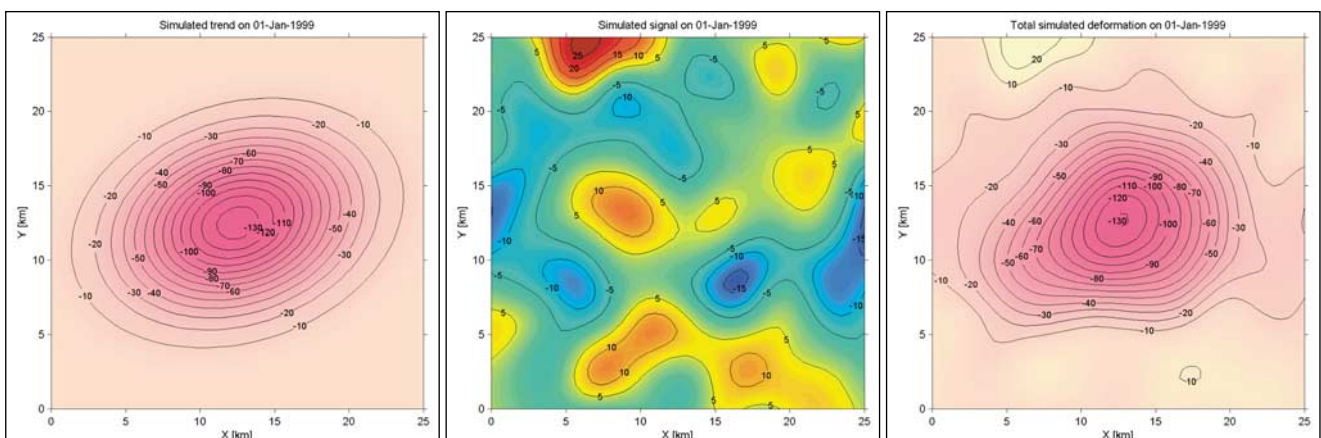
Fig. 4: Contour maps of simulated trend (left), signal (middle) and total deformation (sum of trend and signal; right) on 1 January 1999. All contour labels are in mm.

Tab. 1: Characteristics of simulated subsidence

subsidence velocity bowl center	–10.0 mm/yr
start time subsidence	1 June 1985
half long and short axes ellipse	5000 and 3500 m
argument long axis	80 gon
horizontal position bowl center	exactly in the middle of area of 25 × 25 km
deformation signal	$\sigma_g = 2\ \text{mm}/\sqrt{\text{yr}}$ $L_g = 3\ \text{km}$

maps of this subsidence for 1 January 1991 (5.5 years after the start), while Fig. 4 shows contour maps for 1 January 1999 (13.5 years after the start). Note that due to the simulated deformation signal, there is some small *uplift* in the northwestern part of the area for 1 January 1999. From the figures it seems that the contribution of the signal to the total subsidence can range up to 20 % at some locations.

6.2   Simulated observations

Precise leveling data are simulated for the time span 1983–1999 at five epochs, at a regular interval of four years. The leveling network is a regular grid of lines that completely covers the area of 25 × 25 km, with point distances of 3125 m. In the center of the subsidence area even points are added which are halfway the leveling trajectories, see Fig. 5 (left). This dense and regular leveling network consisting of 121 points connected by 184 observations will probably yield very good results, but is very expensive to measure and maintain it on a regular basis (450(!) km of leveling per epoch). In the simulations it will be referred to as network *L*.

In addition to leveling data, InSAR-derived vertical displacement data are simulated for varying time intervals. It is assumed that these displacement maps cover the same time span as the leveling data, so from 1983 to 1999. We assume to have four InSAR maps available that each cover the 4-year time interval between two leveling epochs, i. e. 1983–1987, 1987–1991, 1991–1995 and 1995–1999. Note that these four maps can – without loss of information – be transferred to four maps that have for example a *common* start date, i. e. 1983–1987, 1983–1991, 1983–1995 and 1983–1999. So in the simulations we could also have used this latter set of maps. The solution using either the first or the latter set will be exactly the same, since the correlation between the maps is properly accounted for in the adjustment. Each displacement
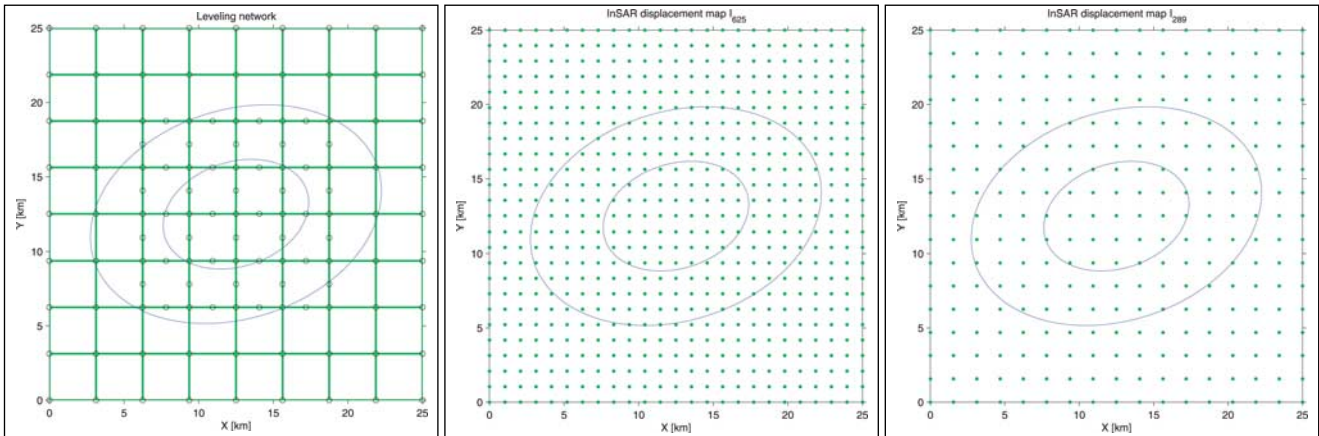
Fig. 5: Simulated data: leveling network L (left), InSAR displacement map I_{625} (middle) and InSAR displacement map I_{289} (right). In the figures also the contours of the subsidence bowl (trend) at one and two times the length of the axes are plotted.

map covers the subsidence area of 25×25 km in the form of a regular grid. In the simulations we varied the spacing (resolution) of this grid:

■ *Network I_{625}* (see Fig. 5; middle), a grid with a spacing of $1/3 \times 3125$ m (the distance between points in the leveling network) = 1041.67 m. This corresponds to $25 \times 25 = 625$ points for the complete subsidence area. Note that this spacing is much larger than the size of a resolution cell of real InSAR displacement data, which is between 25 m (conventional InSAR) and 160 m (permanent-scatterer InSAR). Due to computer memory overflow it is not possible to use very dense grids covering an area of 25×25 km. It is however expected that relatively sparse grids are sufficient for this type of (smooth) deformation.

■ *Network I_{289}* (see Fig. 5; right), a grid with a spacing of 1.5 times the spacing of network I_{625}, i. e. 1562.5 m. (Note that this distance corresponds to the distances between the leveling points of network L in the center of the subsidence area.) This spacing corresponds to $17 \times 17 = 289$ points for the complete subsidence area, and this number is only 46 % of the number of points of network I_{625}.

With the horizontal positions of the leveling and InSAR points extracted from the network configurations, the systematic component of the observations was generated using the simulated vertical deformations. Note that the initial heights of the leveling benchmarks and the shifts of the InSAR displacement maps were simulated as zero values. In addition to this systematic component, for all leveling and InSAR observations a random error was generated in order to simulate measurement noise and noise due to point instabilities. For this purpose again the random generator of Matlab was used. The leveling measurement noise was generated with a standard deviation of 0.7 mm$/\sqrt{\text{km}}$. For the InSAR data we generated two data sets with different measurement noise in order to investigate the effect of the presence of atmospheric artifacts. For both sets a phase standard deviation of 3 mm

was chosen for all points. For the atmosphere-biased map the observations were generated with an additional random error for atmospheric artifacts, having a standard deviation of 1 cm and a correlation length of 5 km. The standard deviation of leveling point noise was chosen as 0.6 mm$/\sqrt{\text{yr}}$, being a realistic assumption conform Wyatt (1989) or Kenselaar and Martens (2000). Since InSAR point noise is usually larger than leveling point noise (Houtenbos 2003), a value of 1.2 mm$/\sqrt{\text{yr}}$ was assumed for the InSAR point noise.

The characteristics of the simulated observations are summarized in Tab. 2.

Tab. 2: Characteristics of simulated observations

leveling networks	1983, 1987, 1991, 1995, 1999
InSAR displacement maps	1983–1987, 1987–1991, 1991–1995, 1995–1999
measurement noise leveling	$\sigma_{w_t} = 0.7$ mm$/\sqrt{\text{km}}$
measurement noise InSAR	$\sigma_\phi = 3$ mm ($\sigma_a = 1$ cm, $L_a = 5$ km)
point noise	$\sigma_{b_i} = \begin{cases} 0.6 \text{ mm}/\sqrt{\text{yr}} \text{ (leveling)} \\ 1.2 \text{ mm}/\sqrt{\text{yr}} \text{ (InSAR)} \end{cases}$

6.3 Simulated processing strategies

In a search for more efficient monitoring strategies we formulated some strategies for the processing of the simulated leveling and InSAR data. The central question hereby is: how accurate can a certain strategy recover the true subsidence? Since we have simulated the true subsidence, the accuracy of a certain strategy can be assessed by comparing the estimated subsidence at a certain location/epoch with its simulated counterpart. This comparison is conducted on a grid of 49 by 49 (= 2401) points spanning the subsidence area of 25×25 km. The following leveling/InSAR strategies are considered:

1. leveling only based on 5 networks L (L);
2. InSAR only based on 4 maps I_{625} (I1);
3. InSAR only based on 4 maps I_{289} (I2);
4. InSAR only based on 4 maps with atmospheric artifacts I_{625}^a (I3);
5. leveling based on 3 networks integrated with InSAR based on 4 maps with atmospheric artifacts I_{625}^a (L/I3).

The choice of these strategies is motivated as follows. The leveling-only strategy in which network L is surveyed every four years is the most expensive strategy but has been included since a leveling-only based strategy is the usual approach for the monitoring of subsidence due to gas extraction. The second and third strategies are InSAR-only based on atmosphere-free displacement maps. From these strategies it immediately follows how well InSAR is able to recover the subsidence, as compared to leveling only. The fourth strategy is also an InSAR-only strategy, but then based on atmosphere-biased displacement maps. In the fifth strategy the four atmosphere-biased InSAR maps are combined with three leveling epochs.

6.4 Results and discussion

The relevant results of the processing of each strategy are summarized in Tab. 3.

Tab. 3: Results processing

	L	I1	I2	I3	L/I3
F-test quotient	0.94	1.00	0.98	0.97	0.97
% of discrepancies < 5 mm, at 1 January 1999	83.9	89.3	68.1	67.8	92.8
precision subs. velocity center (mm/yr)	0.5	0.5	0.5	1.2	0.6
redundancy	793	2489	1145	2489	2921
number of epochs	5	-	-	-	3
number of maps	-	4	4	4	4

In the table first the F-test quotient is given, which is defined as the ratio of the F-test (overall model test) statistic with the critical value of the test. The expectation of this F-test quotient is 1. Tab. 3 shows that for all strategies this quotient is indeed very close to 1, and this is understandable because we simulated the observations, without adding (gross) errors (aside from the random errors). This is also a check that we simulated the data in a correct way.

The second row in Tab. 3 shows the results of the comparison of the estimated subsidence according to each strategy, with our simulated subsidence, in fact the ground truth. In the table the (relative) number of the 2401 grid points is given for which the estimated subsidence agrees within 5 mm with the simulated subsidence at those points. These discrepancies have also been interpolated for the subsidence area and are visualized as contour maps in Figs. 6, 7 and 8. Note that these graphs

and also the percentages in Tab. 3 are given for 1 January 1999, the last observed epoch. An exception to this is the contour map left in Fig. 6, which visualizes the discrepancies on 1 January 1991, halfway the time span 1983–1999. This map has been included to demonstrate that the discrepancies generally grow in time. By evaluating the discrepancies only for the last epoch, 1 January 1999, the percentages can be considered as safe lower bounds. In case of the leveling-only strategy L this lower bound is 84 %. In case of InSAR only (strategies I1 and I2) it follows that the four I_{625}-maps (with a spacing of about 1042 m) are able to recover the subsidence very precisely: for almost 90 % of the area the subsidence is recovered within 5 mm. However, when the spacing of the maps is increased (about 1563 m; in case of the I_{289} maps) this percentage is reduced to about 68 %. Fig. 7 visualizes the discrepancies for both strategies. Note that with an even smaller spacing than of the I_{625}-maps we probably would have obtained a percentage close to 100 %, but this strategy has not been taken into account as due to computer memory overflow problems. The displacement maps in strategies I1 and I2 are simulated without atmospheric errors. When we use the atmosphere-biased I_{625}^a-maps (strategy I3) the result becomes much worse: for only 68 % of the area the recovered subsidence is within 5 mm of the ground truth, versus 90 % for strategy I1, in which the maps have the same spacing as in strategy I3. The left contour map in Fig. 8 visualizes these large discrepancies. The map shows that the discrepancies may be up to 20 mm.

Based on the good performance of the InSAR-only strategy I1 versus the performance of the leveling-only strategy L, it is expected that an integration of these maps with leveling data would barely improve the InSAR-only results. So this strategy was not tried. Another situation applies to the atmosphere-biased InSAR data; for these maps an integration with leveling data might be worthwhile. Hence in strategy L/I3 the atmosphere-biased I_{625}^a-maps are combined with leveling data. However, for this integration we only used three leveling networks (at epochs 1983, 1991 and 1999), since taking all five networks would still lead to a very expensive solution. This integrated L/I3-strategy indeed resulted in a significant improvement: for 93 % of the area at 1 January 1999 the subsidence could be recovered with an accuracy better than 5 mm, thus an improvement of about 25 % compared to the InSAR-only strategy I3. The right contour map in Fig. 8 visualizes the discrepancies of the L/I3-strategy.

These simulations demonstrate that an integration of leveling and InSAR data only leads to better results when the InSAR data are of minor quality due to for example atmospheric artifacts. Otherwise one may rely on InSAR only for this type of subsidence monitoring. As shown in Tab. 3, the precision of the estimated subsidence *velocity* is in the integrated case comparable to the precision of the velocity when either good InSAR data or frequently surveyed leveling data are used: about 0.5 mm/yr.

Fig. 7: Discrepancies between estimated and simulated subsidence for 1 January 1999 using the I1-strategy (left) and the I2-strategy (right). Contours are plotted for each 5 mm difference.
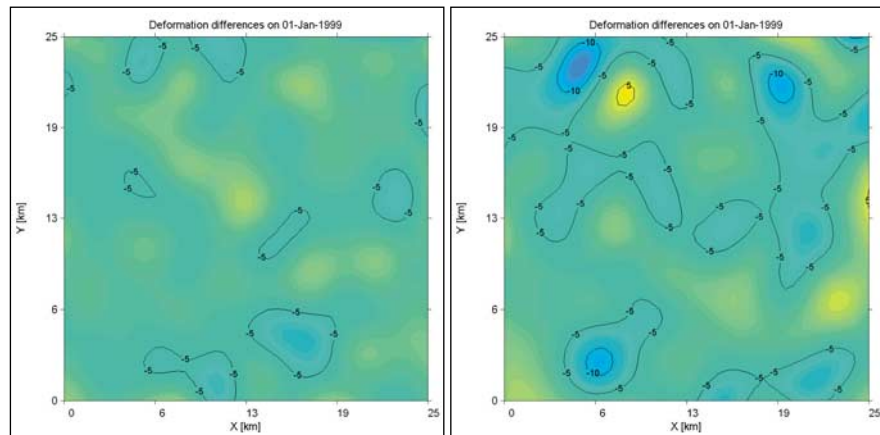
Fig. 8: Discrepancies between estimated and simulated subsidence for 1 January 1999 using the I3-strategy (left) and the L/I3-strategy (right). Contours are plotted for each 5 mm difference.
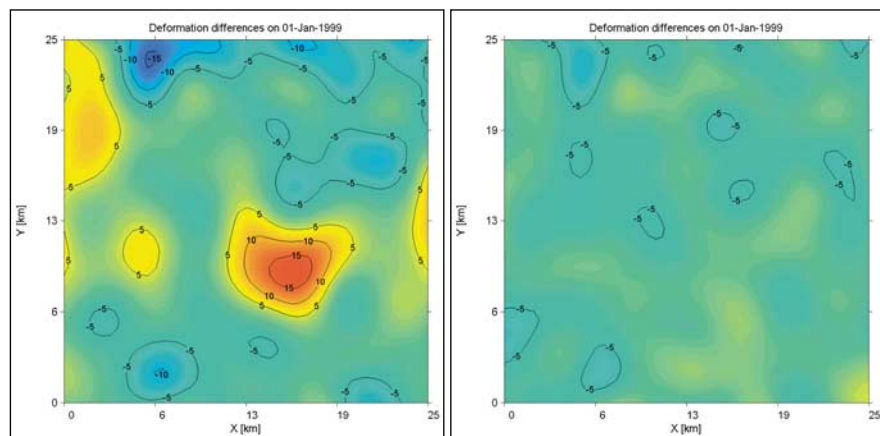
Fig. 6: Discrepancies between estimated and simulated subsidence for 1 January 1991 (left) and 1 January 1999 (right) using the L-strategy. Contours are plotted for each 5 mm difference.
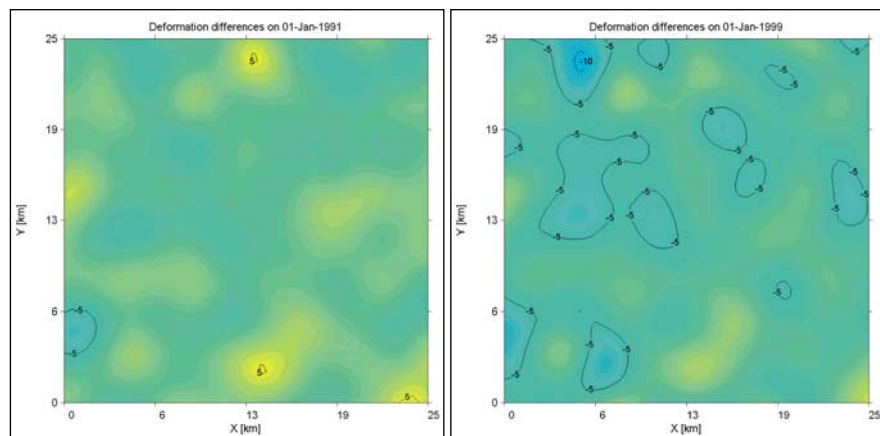
7   Conclusions

There are several advantages of the approach to continuous spatio-temporal modeling of land subsidence due to gas extraction as described in this article:

- It allows for a relatively *easy integration* of measurement techniques, at observation level. Hereby it is not necessary that the different measurement techniques occupy the same points or are observed at the same epochs (although this was the case in the simulations).
- It enables rigorous *statistical testing* of all observations, even those observations that are not redundant when considered as individual data sets.

- In contrast to many other deformation modeling schemes, the approach does not require *stable reference points.*

In this article it has furthermore been demonstrated that despite its benefits (high spatial resolution, relatively low costs), InSAR is currently not yet a fully reliable technique for the precise monitoring of deformations due to gas extraction. Leveling data remain necessary, especially when the InSAR displacement data are contaminated with atmospheric errors or at places where no coherent InSAR data are available, e. g. due to vegetation. In addition, leveling data are indispensable for the detection of deformations that started before 1992, the year the InSAR data

were archived for the first time. The development of the permanent-scatterers InSAR technique is promising, since the problems of low coherence and atmospheric errors are being tackled. However, because the number and location of the permanent scatterers cannot be predicted with this technique, leveling may still be necessary in areas with too few permanent scatterers.

Acknowledgements

References

Baarda, W.: A testing procedure for use in geodetic networks. Netherlands Geodetic Commission, Publications on Geodesy, New Series, 2(5), 1968.

Baarda, W.: S-transformations and criterion matrices. Netherlands Geodetic Commission, Publications on Geodesy, New Series, 5(1), 1973.

Ferretti, A., C. Prati and F. Rocca: Permanent scatterers in SAR interferometry. IEEE Transactions on Geoscience and Remote Sensing, Vol. 39, No. 1, 8–20, 2001.

Hanssen, R. F.: Radar interferometry: data interpretation and error analysis. Kluwer Academic Publishers, Dordrecht, 2001.

Hanssen, R. F., and A. Ferretti: Deformation monitoring by satellite interferometry. GIM International, September, 52–57, 2002.

Hanssen, R. F., D. Moisseev and S. Businger: Resolving the acquisition ambiguity for atmospheric monitoring in multi-pass radar interferometry. Proc. Int. Geoscience and Remote Sensing Symp. (IGARSS), Toulouse, France, 21–25 July, 4 pages cdrom, 2003.

Houtenbos, A. P. E. M.: The quantification of subsidence due to gas extraction in the Netherlands. Proc. 6th Int. Symp. on Land Subsidence (SISOLS), Ravenna, Italy, 24–29 September, 177–189, 2000.

Houtenbos, A. P. E. M.: *Personal communication*, 2003.

Kenselaar, F., and M. Martens: Spatial temporal modelling of land subsidence due to gas extraction. Proc. 6th Int. Symp. on Land Subsidence (SISOLS), Ravenna, Italy, 24–29 September, 383–396, 2000.

Kenselaar, F.: A testing procedure for subsidence analysis. Proc. 10th FIG Int. Symp. on Deformation Measurements, Orange, USA, 19–22 March, 40–49, 2001.

Kenselaar, F., and R. Quadvlieg: Trend-signal modelling of land subsidence. Proc. 10th FIG Int. Symp. on Deformation Measurements, Orange, USA, 19–22 March, 336–345, 2001.

Massonnet, D., and K. Feigl: Radar interferometry and its application to changes in the Earth's surface. *Review of Geophysics*, 4, 441–494, 1998.

Wackernagel, H.: *Multivariate geostatistics: an introduction with applications.* Springer-Verlag, Berlin-Heidelberg, 1998.

Wyatt, F. W.: Displacements of surface monuments: Vertical motion. *Journal of Geophysical Research*, 94, 1655–1664, 1989.

Author's adress
Dr. Dennis Odijk
Department of Earth Observation and Space systems
Delft University of Technology
P. O. Box 5058, 2600 GB Delft, The Netherlands
d.odijk@lr.tudelft.nl